# II.2
# Spin-Polarized Scanning Tunneling Microscopy

WULF WULFHEKEL, UTA SCHLICKUM, AND JÜRGEN KIRSCHNER

We present an overview of spin-polarized scanning tunneling microscopy (Sp-STM). As in STM, the electron density near the sample surface can be imaged. In addition, Sp-STM allows us to map the spin polarization. Thus, information on the magnetic configuration of the sample surface can be gathered. Three imaging modes are currently being used: the constant-current mode, the spectroscopic mode, and the differential magnetic mode. The principles of the three modes are explained, and their advantages and limitations are discussed in the framework of imaging ferromagnetic and antiferromagnetic surfaces of bulk materials and thin film systems. Further, two approaches for controlling the spin direction of the tip apex, i.e., the sensitive spin component, are discussed. Surface or interface magnetic anisotropies at the tip apex may be used to align the axis of sensitivity or alternatively, the shape anisotropy of the whole tip may determine the spin direction. Finally, it is demonstrated that Sp-STM can be used beyond magnetic imaging. Valuable information on the spin resolved electronic structure or on the fundamental processes of spin-polarized tunneling may be obtained.

## 1 Introduction

In scanning tunneling microscopy (STM), the electron charge is used to carry information in the imaging process. The small tunneling current between the tip and the conductive surface is used as a feedback parameter to move the tip. During scanning in the constant current mode, the apex of the tip is held on equi-current lines several Å above the sample surface by the current feedback mechanism. In first approximation, i.e., in the Tersoff–Hamann model [1,2], these lines correspond to the lines of constant charge density of the sample surface probed by the tip apex. A plot of the $z$-coordinate, i.e., the coordinate perpendicular to the overall sample surface, as a function of the position $x$ and $y$ in the surface plane is therefore called a topographic STM image and reflects the spatial distribution of the density of states of the electrons [3]. In the case of a sharp apex, individual atoms can be resolved in topographic images [4]. In the above picture, the spin of the electron has been neglected. For most materials, this simplification is well justified as the electron

density does not depend on the spin of the electron. For ferromagnetic or antiferromagnetic materials, however, the density of states is spin-split into majority and minority states. A net spin polarization is present in the atoms and the individual atoms carry a magnetic moment. In spin-polarized STM (Sp-STM) the tip itself is a source of spin-polarized electrons. Information on the spin polarization of the sample surface may be obtained via the spin-dependent tunneling process between tip and sample. In the case that the spin-dependent part of the tunneling current can be separated from the spin-independent part, it is possible to obtain information on the spin- or magnetic configuration of a sample surface with the same lateral resolution as topographic information, i.e., with atomic resolution. Thus, Sp-STM is the magnetic imaging technique with ultimate lateral resolution, which for the first time allows the study of the magnetic configuration of antiferromagnets in real space. Examples for imaging both ferromagnetic and antiferromagnetic surfaces are given, after the principles of spin-polarized tunneling are introduced in detail. Three different approaches to separate spin information from the tunneling current are discussed, and examples are given for all three imaging modes. The potential of the different techniques is illustrated and their advantages and disadvantages are discussed. Further, we focus on tip preparation and finally show that Sp-STM can be used beyond magnetic imaging to learn more about spin-split density of states and the mechanism of spin-polarized tunneling, per se.

## *1.1 Spin-Polarized Tunneling*

The principle of operation of Sp-STM is based on the fundamental property of ferromagnets and antiferromagnets—that their magnetic moment is related to an imbalance in occupation of electrons of different spins. Due to the spin-sensitive exchange interaction, the density of states splits up into minority and majority densities (see Figure (1a)). The imbalance causes a spin polarization. This is in contrast to paramagnetic substances, where the distributions of spin-up and spin-down electrons are identical and no spin polarization is present. The splitting

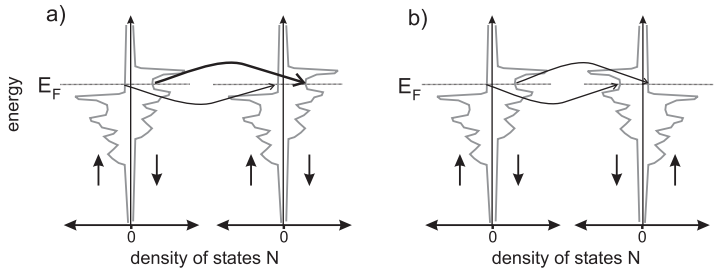


FIGURE 1. Tunneling between two ferromagnetic electrodes that show a spin split density of states $N$ ($\uparrow/\downarrow$ indicate majority/minority states). In **(a)** and **(b)** the magnetization of the two electrodes is parallel and antiparallel, respectively. The conductivities for tunneling from the left to the right electrode are indicated by arrows.

of the density of states has immediate consequences on the tunneling current as pioneering field-emission experiments with ferromagnetic tips have shown [5, 6]. During the tunneling process from the ferromagnetic tip into the free states of the vacuum, the spin polarization of the density of states in the tip is partly transferred to the emitted electrons and a spin-polarized current was observed. This can easily be understood using a simple model. As the tunneling barrier, i.e., the potential step of the work function in front of the tip, is not spin dependent, the transmission probability through the barrier does not depend on the electron spin. The observed polarization is just a consequence of the different number of states for minority and majority electrons in accordance with Fermi's golden rule: the more states are allowed to tunnel, the higher the resulting tunneling current. Therefore, the tunneling current from a spin-polarized tip is spin-polarized according to the imbalance in spin of the involved states.

This effect alone is not enough to obtain spin information in STM, since the spin polarization of the tunneling current is not directly accessible. The only measured parameter is the magnitude of the current. It was Jullière [7] who discovered that when electrons tunnel between two ferromagnets, not only the current is spin-polarized but also the magnitude of the current is influenced. The phenomenon was therefore referred to as the tunneling magnetoresistance (TMR) effect. In his experiment, two magnetic films were separated by a thin insulator film to form a planar tunnel junction. The two magnetic films were chosen to have different coercive fields. This permitted Jullière to align their magnetization parallel or antiparallel as a function of an applied magnetic field. Jullière found that the tunneling conductance $G$ (and by this the resistance) depends on the relative orientation of the magnetization of the two layers. For parallel orientation, $G$ was higher than for antiparallel orientation. This finding can be explained on the basis of a simple model for tunneling. As above, we neglect any spin dependence in the transmission through the barrier and focus solely on the electronic properties of the two electrodes. Under the assumption of a small bias voltage across the junction and in the absence of spin-flip scattering during the tunneling process, the electrons in the ferromagnets near the Fermi energy determine the tunneling conductance of the junction. For a parallel orientation, the majority/minority electrons of the first electrode tunnel into the majority/minority states in the second electrode, respectively, as sketched in Figure 1(a). Using Fermi's golden rule, the conductance $G$ is proportional to the density $N$ of initial (i) and final (f) states at the Fermi edge. Combining both spin channels, the conductance for parallel oriented magnetizations is given by

$$G_{\uparrow\uparrow} \propto N^i_\uparrow N^f_\uparrow + N^i_\downarrow N^f_\downarrow . \tag{1}$$

For the antiparallel orientation, electrons of majority character in one electrode tunnel into states of minority character in the other electrode and the conductance is given by a mixed product:

$$G_{\uparrow\downarrow} \propto N^i_\uparrow N^f_\downarrow + N^i_\downarrow N^f_\uparrow . \tag{2}$$

These two conductivities are in general not identical, leading to a variation of the tunneling current with the magnetic configuration of the electrodes. Slonczewski treated the problem of spin-polarized tunneling more rigorously [8]. Neglecting higher-order spin effects like spin accumulation, he calculated the dependence of $G$ on the angle $\theta$ between the magnetization of the two electrodes. With the spin polarization $P = (N_\uparrow - N_\downarrow)/(N_\uparrow + N_\downarrow)$, the conductance is given by

$$G = G_0(1 + P^i P^f \cos\theta). \tag{3}$$

The cos $\theta$ dependence is rigorous, reflecting the quantum mechanical rotation behavior of the spin $\frac{1}{2}$ tunneling electrons. Slonczewski's prediction for the angular dependence of the TMR effect was later experimentally confirmed [9].

In general, if a finite bias is applied, all states between the two Fermi levels are involved in tunneling. They have to be weighted according to their tunneling probability through the barrier, which is, e.g., energy dependent. This scenario is more complex but $G$ can be expressed using effective, i.e., correctly weighted, densities or polarizations.

## 2 Imaging Modes

Already in 1988, Pierce suggested setting up a STM that uses the TMR effect to image the sample magnetization with high lateral resolution [10]. He suggested two different approaches to create a spin-polarized current—the use of ferromagnetic tips and the possibility to photo-excite spin-polarized carriers in GaAs tips. While we focus on the first, the latter was realized by Suzuki et al. [11]. In the latter approach, circularly polarized light is used to excite spin-polarized carriers into the conduction band of the tip that then tunnel into the sample. The spin polarization of the electrons can be selected by the helicity of the light. By modulating the helicity of the light, modulations in the tunneling current are induced due to spin dependent tunneling. The modulations were detected with a lock-in amplifier to separate spin information from topographic information. The optical modulation technique, however, suffers from a rather low contrast and an unintended additional magneto-optical contrast of low resolution. Only a few studies on domain patterns have been published using this technique. Note that the inverse effect, i.e., the tunneling form a ferromagnetic Ni tip into GaAs followed by the emission of polarized light, was experimentally demonstrated [12]. Much more successful was the development of Sp-STM using ferromagnetic tips. In his pioneering publication, Pierce suggested three different imaging modes of Sp-STM which have been all realized experimentally and which are discussed in detail below. A theoretical description of the three imaging modes was given recently by Heinze et al. [13].

### *2.1 The Constant-Current Mode*

In the constant-current mode of Sp-STM, a spin-polarized tip is scanned over a spin-polarized surface in the conventional constant-current mode of STM. In this

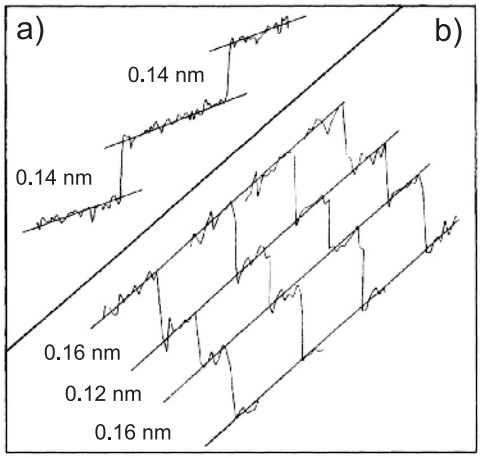


FIGURE 2. Constant current line scans of the Cr(001) surface with **(a)** a W tip and **(b)** a $CrO_2$ tip. The variation of the step height in (b) is a result of spin-polarized tunneling. Figure used with kind permission of Wisendanger [14].

case, the images contain mixed topographic and spin information. Wiesendanger et al. were the first to use this imaging mode. They reported on spin-polarized vacuum tunneling at room temperature between a ferromagnetic $CrO_2$ tip and the (100) surface of the layer-wise antiferromagnetic bcc Cr [14]. Using a non-magnetic W tip, topographic line-scans revealed atomic steps on the Cr surface of the expected step height of 0.14 nm (see Figure 2(a)). When, however, the experiment was repeated with ferromagnetic $CrO_2$ tips, alternating step heights of 0.16 and 0.12 nm were observed (see Figure 2(b)). This was attributed to the TMR effect between the ferromagnetic tip and the antiferromagnetically ordered Cr terraces. When the spin polarizations of the tip and the Cr terrace atoms are parallel, the tunneling current is enhanced (see Eq. (3)). In the constant current mode of the STM, the tip is retracted by a small amount (0.02 nm). Due to the layer-wise antiferromagnetic order of Cr(001) [15], the spin polarization of the tip and the Cr atoms is antiparallel on the adjacent atomic terrace. The TMR effect leads to a reduction of the current and the STM tip approaches. This mechanism results in alternating step heights seen with a spin-polarized tip and allowed an indirect observation of the sample spin polarization. No separation of topography and spin information could, however, be obtained in this approach and reference measurements had to be acquired with non-magnetic tips. Further, the interpretation of the data was based on the assumption that both the spin polarizations of the tip apex and the Cr sample were oriented along the surface normal. As we know now, this assumption was wrong, at least for the Cr surface [16].

Recently, the constant-current mode was used to obtain information on the sample spin on the atomic scale. Heinze et al. used Fe-coated W tips to resolve the antiferromagnetic order in Mn films on W(110) [17]. When imaging the Mn film with nonmagnetic tips, the bcc(110) $1 \times 1$ unit cell could be observed. When using a spin-polarized tip, a spin contrast is added in the topographic image and the unit cell expanded to a $c(2 \times 2)$ cell, reflecting the magnetic unit cell. Note,

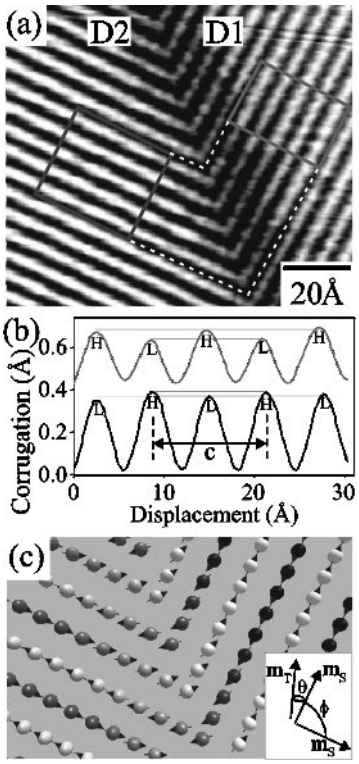


FIGURE 3. **(a)** Constant current images of the $Mn_3N_2(010)$ taken with a spin-polarized tip and **(b)** averaged line scans of the corrugation in the domain D1 (top) and D2 (bottom). **(c)** Model of the surface spins. Reprinted figure with permission of A.R. Smith [18]. Copyright 2002 by the American Physical Society.

however, that the additional corrugation is damped, as the structures are smaller than the lateral resolution of the tunneling process [17].

Since in the constant current mode, the contrast is largely due to the topography and only a small variation of the tip-sample distance is related to the spin polarization, it has mostly been used on surfaces of constant electronic structure like simple metallic surfaces with small corrugation. It may, however, also be applied to complex materials with large topographic corrugation in the unit cell. Yang et al. have used Fe- and Mn-coated tips to study the spin configuration of the $Mn_3N_2(010)$ surface [18]. Figure 3 shows constant current images with two crystallographic domains. Clearly a row structure can be seen that was related to Mn planes in $Mn_3N_2$. With spin-polarized tips, a modulation of the height of the rows was detected on both domains (see Figure 3(b)) that reflects the antiferromagnetic coupling between the Mn planes. Due to the different orientation of the Mn planes and by this the different alignment of the Mn moments, the modulation in the topography is different on the two domains. The higher the component of the Mn spins along the tip magnetization, the larger the modulation of the corrugation. By taking the average and the difference of two line scans that are shifted by half the magnetic periodicity, Yang et al. managed to separate the spin independent and spin dependent part of the corrugation.

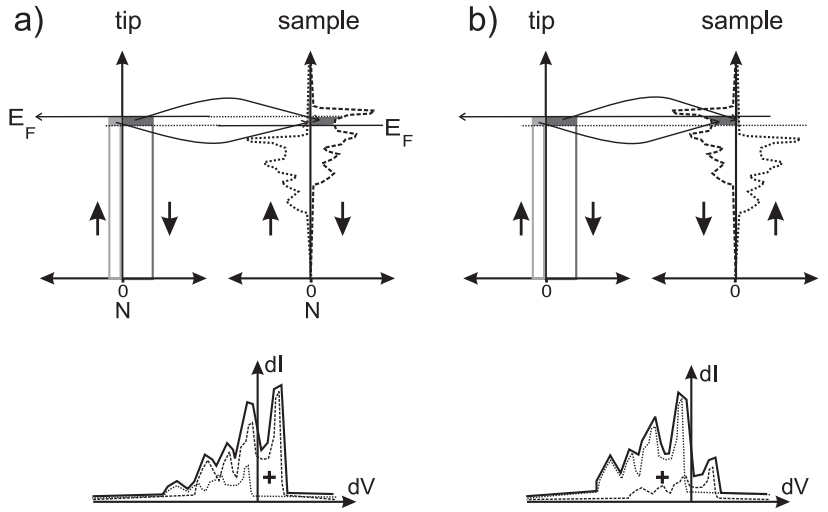


FIGURE 4. Tunneling between a ferromagnetic tip and sample for **(a)** parallel and **(b)** antiparallel magnetization of both. The corresponding differential conductivities $dI/dU$ as function of bias $U$ are sketched below.

This method, however, is only suitable for systems with a known magnetic unit cell.

## *2.2 The Spectroscopic Mode*

A mode that under certain circumstances allows separation of topographic information from spin information is spin-polarized scanning tunneling spectroscopy. It was initially suggested by Pierce [10] and Stroscio et al. [19] and was first realized by Bode et al. [20]. It uses the fact that the spin polarization of the sample density of states is a function of the energy.

For simplicity, we assume that the density of states in the tip is featureless, i.e., constant. The spin polarization of the tip states is constant as well. When a finite bias is applied between tip and sample, a set of states may contribute to the tunneling. As illustrated in Figure 4(a), a positive sample bias $U$ leads to the tunneling of all tip states between $E_{F_t} - U$ and $E_{F_t}$ to empty states in the sample between $E_{F_s}$ and $E_{F_s} + U$. Using the same simple approximation for the tunneling current as above, the tunneling current is proportional to the density of states of the sample integrated from $E_{F_s}$ to $E_{F_s} + U$ for both spin channels and weighted by the (constant) density of states of the tip. In this approximation, the differential conductance $dI/dU$ as function of the sample bias $U$ is simply given by the spin split density of states of the sample weighted by the constant tip density of states [2, 13]. In the example of Figure 4a, where the tip and the sample magnetization are parallel, the measured $dI/dU$ is dominated by the minority density of states of the sample and contains only little information on the majority density of states, as the tip states are mainly of minority character. When the sample is magnetized in opposite

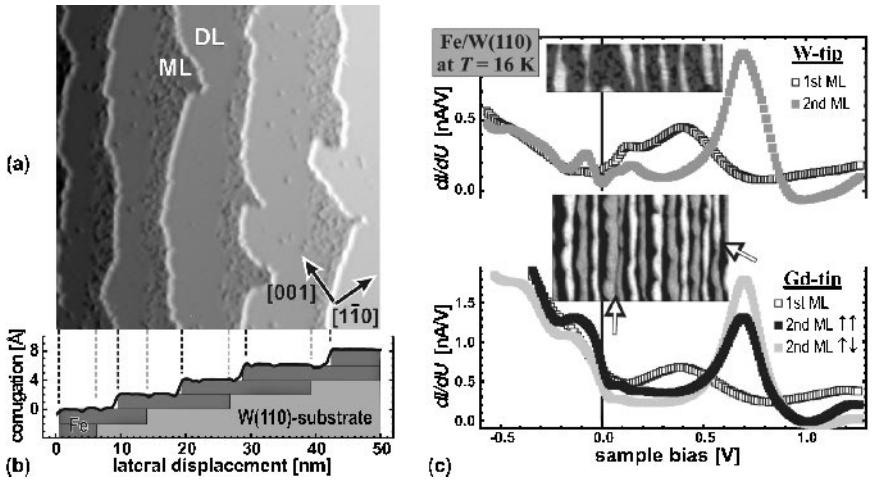


FIGURE 5. Topographic image **(a)** and line scan **(b)** of $\approx$ 1.5 ML Fe on W(110). **(c)** Differential conductance of ML and DL areas taken with a W tip (top) and a Gd tip (bottom) as function of the sample bias. The insert shows maps of the differential conductance revealing magnetic information in case of Gd tips. Figure kindly provided by M. Bode.

direction to the tip, the balance is changed and the contribution of majority density of states in the differential conductance dominates (see Figure 4(b)). The resulting differential conductance is simply a linear combination of the minority and majority density of states depending only on the relative orientation of tip and sample magnetization. Therefore, the characteristic energies, e.g. the position of peaks in the $dI/dU$ spectra, do not change, whereas the peak heights vary with the sample magnetization.

In the pioneering experiment by Bode et al., the height of the spin-split surface state of Gd(0001) in laterally resolved $dI/dU$ spectra was used to obtain magnetic information [20].

Figure 5 shows an example for magnetic contrast obtained with Sp-STM using Gd-coated W tips. The tips show a sensitivity for the out-of-plane magnetization, which suggest that they are magnetized along the tip axis. When Fe is deposited onto W(110) at 300 K followed by annealing to elevated temperatures, the Fe films grow in the step-flow growth mode [21]. For coverages between one and two mono-layers (ML), this results in alternating mono-layer and double-layer (DL) stripes as depicted in the topographic image of Figure 5(a) and the schematic sketch of Figure 5(b). As has been shown by Elmers et al., the ML stripes have an in-plane magnetization, while the DL stripes are magnetized out-of-plane [21]. When performing tunneling spectroscopy on these samples with W tips, two different $dI/dU$ spectra were observed (see Figure 5(c)), reflecting the different electronic structure of the ML and the DL areas. When plotting the differential conductance at 0.68 V as a function of the tip position, a map of the local differential conductance (see inset in Figure 5(c)) shows the DL areas as bright and the ML areas as dark patches, since $dI/dU$ of the DL is much higher than that of the ML at the

chosen voltage. When using a ferromagnetic, Gd-coated tip, the overall shape of the $dI/dU$ spectra changes little, but the DL stripes display two distinct types of spectra. Due to spin-polarized tunneling, one spectrum has a higher differential conductance around the peak at 0.68 V while the other has a higher differential conductance at around $-0.2$ V. The first is the spectrum for antiparallel tip and sample magnetization and the latter for parallel. When plotting $dI/dU$ at 0.68 V as a function of position, a magnetic contrast is visible in the maps of the local differential conductance. Besides the contrast between DL and ML stripes mentioned above, an additional contrast between different DL stripes appears (see inset of Figure 5(c)). Neighboring DL stripes have an alternating contrast reflecting an antiferromagnetic alignment of neighboring DL stripes. This confirms the dipolar antiferromagnetic coupling that reduces the stray field energy of the sample similar to stripe domains in perpendicular magnetized films [21, 22].

The magnetic configuration of antiferromagnets can be investigated as well, as Sp-STM is sensitive to the spin polarization at the surface [16]. Figure 6 shows

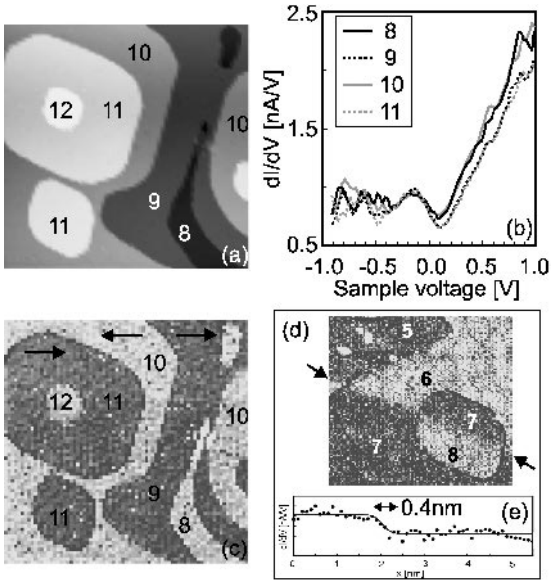


FIGURE 6. STM and SP-STM measurements of 10 ML Mn deposited on Fe(001) at 370 K. These measurements were performed with an Fe- coated W tip. **(a)** $100 \times 100\text{nm}^2$ topographic image ($U = -0.5$ V, $I = 0.5$ nA). Numbers in (a) and (c) denote the numbers of the Mn layers. (b) $dI/dV$ curves as a function of the sample bias voltage obtained on the Mn layers in (a). $dI/dV$ curves obtained on even (odd) Mn layers are shown as solid (dashed) curves, which were numerically obtained from $I(V)$ curves measured at a set point of $U = -0.5$ V, $I = 0.5$ nA. (c) *dI/dV* map at $+0.2$ V measured at the same area as a). (d) *dI/dV* map at $+0.4$ V of 7.2 ML Mn on Fe(001) ($U = -0.6$V, $I = 0.5$ nA, $70 \times 70$ nm$^2$). The magnetic contrast reverses across the hidden step. (e) An averaged line profile across the hidden step in the $dI/dV$ map is shown. Figure kindly provided by T.K. Yamada.

the example of thin Mn films grown on Fe(001). Mn grows in the body centered tetragonal (bct) configuration and shows ferromagnetic coupling within an atomic layer while the different layers couple antiferromagnetically [23–25]. Figure 6(a) shows the topography of the Mn film. Due to imperfect growth, several layers are exposed at the surface. Sp-STM spectra taken with Fe-coated tips on the different layers are shown in Figure 6(b). While the differences between spectra taken on odd (even) layers are minute, the spectra of odd and even layers vary strongly, i.e., the spectra taken on odd and even layers fall into two classes. This reflects the layer-wise antiferromagnetic order of the Mn film, changing the tunneling probability between sample and spin-polarized tip due to the TMR effect. When plotting the differential conductivity at 200 mV as a function of position (see Figure 6(c)), the layer-wise antiferromagnetic order results in alternating bright and dark terraces. Interestingly, the antiferromagnetic order of the Mn film can be disturbed at buried Fe step edges, as will be discussed in detail below. As a result, a magnetic frustration similar to a domain wall is induced in the Mn-film (see Figure 6(d, e)). These walls can be rather sharp. A lateral resolution of 0.4 nm has been claimed by Yamada et al. [25], which is close to the theoretical limit for s-electron tunneling [2].

Sp-STM in the spectroscopic contrast mode has been used in a variety of systems (Gd/W(110), Fe/W(110), Fe/W(100), Fe/Mo(110), Cr(001), Fe/Cr(001), Co/Cu(111), Mn/Fe(001)), with ferromagnetic and antiferromagnetic tips that are sensitive to one in-plane or the out-of-plane component of the spin polarization [16, 20, 22, 25–30].

## *2.3 The Differential Magnetic Mode*

In the differential magnetic imaging mode, the tip magnetization is modulated rigorously to separate the spin information of a sample surface from the topography. In Sp-STM, the nonmagnetic tip is replaced by a bulk ferromagnetic STM electrode. This method was proposed by Pierce [10] as well. First attempts using Ni-tips were of limited success [31]. Only recently was this mode realized to obtain magnetic contrast [32].

The basic concept of this mode is related to Eq. (3). The tip magnetization is periodically reversed, which is equivalent to changing the sign of the spin polarization of the tip apex. In the experimental setup, the magnetization of the tip is reversed by an alternating current through a small coil that is fixed to the tip. The frequency of the alternating current is chosen above the cutoff frequency of the feed back loop of the STM [32]. Thus, the feedback loop only detects the averaged tunneling current $\overline{I} = I_0$ for the two spin polarizations (positive and negative) of the tip apex. The spin-dependent part in the averaged tunneling current cancels out, so that the topographic image contains no magnetic information. With a phase-sensitive lock-in amplifier, the alternating part of the tunneling current $\Delta I$ is detected which is within the Jullière model proportional to $P^i P^f \cos\Theta$. It contains all the spin information. This way, topographic and spin information are

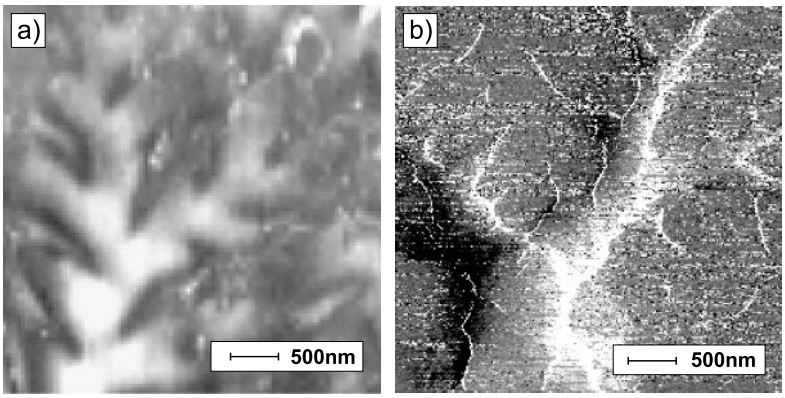


FIGURE 7. **(a)** MFM and **(b)** Sp-STM image of the fractal domain pattern of Co(0001). The scans were performed on the same sample but not on the same area.

separated and an image of the spin component along the magnetization axis of the tip magnetization can be recorded simultaneously with the topography [32].

In the experiment, the alternating magnetic field induced within the coil has to be large enough fully to reverse the magnetization of the tip. The alternating field, however, may also create induction currents in the tunneling loop. For this reason, only extremely soft magnetic materials may be used as tips. Moreover, magnetostriction of the tip during the reversal must be avoided. The initial experiments of Johnson et al. suffered from large magnetostriction of the Ni tip, so that no stable magnetic or topographic imaging was possible [31].

When using tips that are magnetized perpendicular to the sample plane, the out-of-plane component of the spin polarization may be imaged [32]. As an example, the closure domain pattern of Co(0001) is shown in Figure 7. In magnetic force microscopy (MFM) images of the sample magnetization, the fractal domain pattern of Co(0001) is visible. It originates from the partial flux closure of the perpendicular bulk domains at the sample surface [33]. The limited lateral resolution of MFM becomes apparent at the magnification of the image. In contrast to MFM, Sp-STM reveals the full detail of the fractal structure as depicted in Figure 7(b). Ultranarrow 20°-domain walls of 1.1-nm width were observed [34,35], indicating a lateral resolution better than 1 nm.

Bulk in-plane magnetized STM electrodes also allow the imaging of one in-plane component of the spin polarization [36]. The differential magnetic contrast mode was applied to layer-wise antiferromagnetic Mn films on Fe(001), which allows direct comparison to the spectroscopic mode shown above. Figure 8(a) shows a schematic picture of the alignment of the magnetic moments in the ferromagnetic Fe substrate and the antiferromagnetic Mn film. Within the Mn film, the magnetization is reversed in every atomic layer, while the coupling at the Mn-Fe interface is ferromagnetic [37]. When several Mn layers are exposed at the surface, their magnetization points into opposite directions on adjacent Mn terraces due to

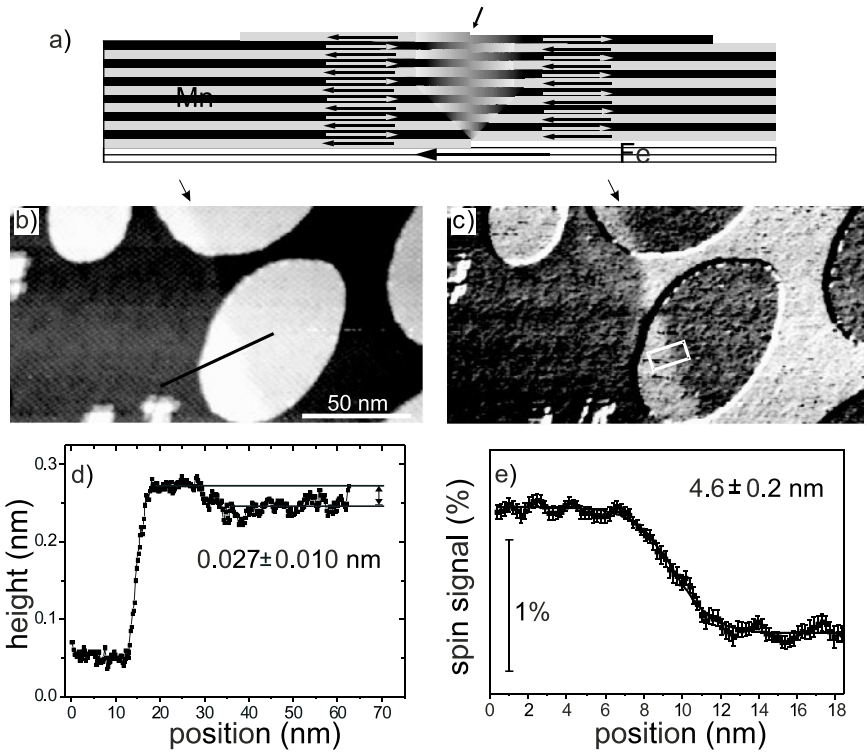


FIGURE 8. **(a)** Schematics of Mn layers overgrowing an Fe substrate step. Above the buried Fe step edge a magnetically frustrated region occurs. Sp-STM image of **(b)** the topography and **(c)** the corresponding spin signal of 11.9 ML Mn on Fe(001). A buried Fe step edge is running almost vertically through the center of the images, indicated by arrows. **(d)** Line profile taken along the line in (b) showing a monatomic Mn step and a step of subatomic height formed by a buried Fe step. **(e)** Line profile (averaged over 70 lines) across the magnetically frustrated region in the Mn film at the position of the box in (c). The solid line represents a fit.

the layer-wise antiferromagnetic order. The situation of the magnetic order above a buried Fe step edges is more complicated. The thickness of the Mn layers on both sides of a monatomic Fe step differs by one ML. Due to the vertical lattice mismatch (bcc Fe versus bct Mn), subatomic steps are formed at the Mn film surface at the position of Fe step edges. An undisturbed layer-wise antiferromagnetic order within the Mn film is not possible when the Mn moments at the interface on both sides of the step edge are aligned in the same direction by the Fe substrate. Instead, Mn layers which meet at the position of the Fe step edge have an opposite spin polarization. This leads to a magnetic frustration similar to a 180° domain wall in the Mn film [25, 38–40].

A region above a buried Fe step edge is shown in Figure 8(b) for the topography and c for the corresponding spin signal. A buried Fe step edge is running almost

**Au: Is this sentence correct?**

vertically through the center of the imaged area (see black arrows). The line profile in Figure 8(d) taken along the line in Figure 8(b)) shows a step of monatomic height between two different Mn terraces (≈0.16 nm) and a step of subatomic height (≈0.018 nm) at the position of a buried Fe step edge. The latter is caused by the different lattice constants of Fe and Mn. In Figure 8(c) clearly the layer-wise antiferromagnetic order between the Mn islands and the Mn layer underneath is visible similar to Figure 6(c). Following the way of the buried Fe step edge, a magnetically frustrated region is formed in the spin signal, where a reversal of contrast appears. Figure 8(e) presents an averaged line profile across the topologically enforced magnetic frustration at the position of the box in Figure 8(c). The measurements indicate that the magnetic frustration has a certain lateral extension. To estimate the wall width at the surface, the experimental profile is fitted with a standart wall profile $tanh(x/w)$. This function is the analytical solution for a one-dimensional domain wall neglecting dipolar energies. The curve is plotted as a solid line in Figure 8(e) and fits the shape of the transition region well. The resulting width ($2w$) was in this case $4.6 \pm 0.2$ nm.

A systematic study of the wall width as a function of the Mn film thickness has shown a widening of these regions with increasing Mn film thickness [40]. The smallest width of 1.2 nm was imaged between the second and third ML Mn and the widest one of $6.9 \pm 0.3$ nm between 18 and 19 ML Mn (see Figure 9). Thicker Mn films could not be investigated due to the phase transition to $\alpha$-Mn resulting in a three dimensional growth and rough surfaces. Neglecting the magnetostatic energy in the antiferromagnet, the width of a 180° domain wall in the Mn film is determined by a competition between the exchange energy and the magnetic anisotropy energy. For the layer-wise antiferromagnetic Cr a wall width of about 120 nm [16] has been found. Assuming an antiferromagnetic exchange proportional to the Néel temperature and a Mn anisotropy similar to that of the 3D ferromagnets, one expects between 20 and 60 nm for the bulk domain wall width in Mn. The pinned domain walls at Fe step edges result, however, in narrow widths at the interface. The driving force for widening of the wall for thicker Mn films is the exchange energy which is gained by approaching the bulk domain wall configuration. Thus, the width of the wall should asymptotically approach its bulk wall width with increasing film thickness. As expected, we observed a widening, but it is linear with no sign of saturation. This is in agreement with the relatively narrow walls when compared to the expected bulk wall width.

To calculate the width of the wall in the Mn film on Fe(001), an effective Heisenberg model with classical spins was used and a fourfold magnetic anisotropy was included. While the values for the exchange coupling constants and the anisotropy constant are well known for bulk bcc Fe [41] the values for bct Mn were estimated. The value for the nearest-neighbor interaction was determined assuming a linear dependence between the ordering temperature and the exchange coupling [41]. For estimating the exchange for the next-nearest neighbor, we assumed a decay of the exchange with increasing distance ($r$) by $r^{-5}$. The resulting estimated coupling constants are depicted in the inset of Figure 9. When taking into account only the nearest neighbor interaction, the modelled walls are too narrow (open squares).

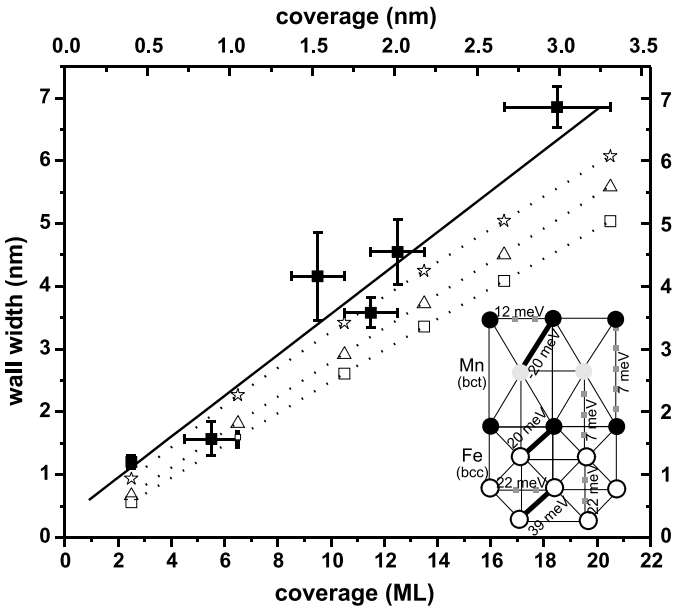


FIGURE 9. The measured wall width as a function of Mn film thickness with linear fit (solid line) together with calculated wall widths of magnetically frustrated regions using the Heisenberg model. The calculated data shown in open squares are obtained by considering only the nearest-neighbor exchange interaction and in open triangles by considering the nearest- as well as the next-nearest-neighbor exchange interaction and the bct structure of Mn. Using the same parameter as in the latter case and reducing the exchange at the interface to 25%, one obtains the values presented in open stars. The insert shows the exchange constants used in the Heisenberg model.

When the nearest- and next-nearest-neighbor exchange interaction were considered, the simulations (open triangles) are closer to the experimental data, but still a small offset occurs. For both calculations the coupling across the interface between Fe and Mn was identical to the one within the Mn film. When reducing the interface coupling to 25%, the agreement to the experimental data is better (open diamonds) which suggest that the exchange interaction at the interface between Fe and Mn may be reduced. This demonstrates that Sp-STM may also provide insight into fundamental mechanisms in magnetism.

The differential magnetic contrast mode was used in polycrystalline Ni, Co(0001), Fe(001) and Mn/Fe(001) [35, 36, 40, 42].

## 3 Tip Preparation

For spin-polarized STM, at least the last atom at the tip apex must have a spin polarization stable in magnitude and orientation. Two different approaches have

been used in the past to reach these conditions. First, the whole tip may consist of a material with a certain spin polarization or a non-magnetic tip is coated with spin-polarized material. These two approaches are discussed below.

## *3.1 Tuning of the Axis of Sensitivity in Thin Film-Coated Tips*

Coated tips are suitable for the constant current and the spectroscopic imaging mode. Most frequently, nonmagnetic W tips are used. To obtain spin contrast, these tips are coated in situ with a thin film of either a ferromagnet or an antiferromagnet. Best results have been reported if the W tips are flashed to high temperatures before coating. This cleans the tip apex from the natural oxide of W and leads to a reproducible but rather blunt tip [43]. When depositing, e.g., an Fe layer of 10 mL on the tip followed eventually by gentle annealing, the tip is covered by either a continuous film or patches of Fe, that show a magnetization along the curved surface of the tip. This direction of magnetization is a consequence of the shape anisotropy of the thin Fe films. Therefore, the tunneling part of the tip has most probably a magnetization in the sample plane and one in-plane component of the magnetization can be imaged [20]. When, however, the tip is coated with a $\approx$10 ML film of Gd, the tips exhibit sensitivity for the out-of-plane component of the spin polarization [22]. This is most likely due to the interfacial magnetic anisotropy of Gd on W that favors magnetization perpendicular to the interface, i.e., at the apex along the tip axis. Both Fe- and Gd-coated tips produce a small magnetostatic stray field at the tip apex that in some cases may influence the magnetic object under investigation [26]. Alternatively, antiferromagnetic Cr [26] or Mn [25] coatings have been used. While the orientation of the spin polarization of the apex is more difficult to control, the tips are mostly free of stray fields. Yamada et al. showed that in antiferromagnetically coated Mn tips, voltage pulses on the tip may even be used to change the direction of sensitivity [44].

## *3.2 Controlling the Magnetization Direction in Bulk Magnetic tips*

Bulk tips are suitable for all three imaging modes. Here, however, we focus on the special necessities of the differential magnetic imaging mode.

The direction of magnetization in bulk magnetic tips is primarily determined by the shape of the tip. For tips that are sensitive to the out-of-plane component of the spin polarization, sharp tips have produced best results [35]. Tips were electrochemically etched from thin CoFeSiB wires of 130 μm diameter. As etching agent, a dilute mixture of HCl and HF was used that was suspended by surface tension as a thin liquid membrane in a Pt ring during etching. The pH value was adjusted so that the formation of silica from the Si in the amorphous wire was prevented. Using low etching currents of the order of 250 μA, pointed tips of cone angles typically between 8° and 15° were created. Due to the large shape anisotropy, a tip magnetization along the tip axis is ensured [45]. When using

the differential magnetic contrast mode, it is important to avoid vibrations due to magnetic switching. The chosen material offers extremely low coercivities in the range of 50 μT and negligible magnetostriction. This ensures virtually vanishing vibrations [45]. While magnetic stray fields cannot be avoided in this configuration, hard magnetic samples could be imaged without problem.

For imaging one in-plane component of the spin polarization, ring-shaped STM electrodes can be used. In these ring electrodes, the magnetization direction lies tangential to the outer perimeter of the ring. Thus, at the bottom of the ring where the tunneling occurs, the magnetization lies in the plane of the sample surface. Because the magnetic flux in an ideal ring is closed, the magnetic stray field is zero. Experimentally, even soft magnetic materials could be imaged [36] using ring electrodes. By choosing the plane in which the ring is oriented, the magnetization direction of the ring is defined and thus the direction of the sensitivity in the surface plane for the measured spin signal is known. Although the rings used as STM electrodes are not sharp, a lateral resolution below 1 nm could be achieved [36,40]. Most likely nanotips exist at the apex which give a high lateral resolution.

To obtain spin contrast, the STM electrodes need to be cleaned in situ, e.g., by Ar sputtering. The contrast can be increased by coating the CoFeSiB tips with several ML of Fe.

## 4 Advantages and Disadvantages of the Different Modes

The different contrast modes all have their specific advantages and drawbacks.

The constant current imaging mode is the simplest imaging mode. It has the advantage that it does not need any sophisticated spectroscopy. It can be carried out with any STM in vacuum that shows a high enough stability. The nonmagnetic tip is replaced either by a ferromagnetic or an antiferromagnetic tip. Both bulk and coated tips can be used. The mode in principle offers atomic resolution. It is well suited to study antiferromagnets and the spin structure in more complex materials. For itinerant ferromagnets, it is, however, less appropriate. As the image consists of mixed topographic and spin information, an unfolding of the two channels is necessary to gain information on the spin configuration. On the atomic scale, this can be done by studying the corrugation with nonmagnetic and spin-polarized tips. The additional corrugation due to the spin is of the order of several picometers. In itinerant ferromagnets, the magnetic domains often extend over the range of a micron. Currently, STM is not able to resolve an additional picometer scale corrugation on these lateral length scales. Further, a small variation of the density of states by contaminations, statistical variation in alloy composition, etc., leads to a corrugation that is hard to distinguish from a spin-induced corrugation in the constant current mode. Therefore, this mode has been used in chemically ordered and single crystalline systems. The use of antiferromagnetic tips in this mode allows avoiding magnetic dipole interaction of the tip and the sample.

The spectroscopic mode is a more sophisticated mode. In samples with a homogeneous density of states, the magnetic signal can be separated from the

topographic information. However, additional studies of the differential conductivity with an unpolarized tip are required. In case the spin polarization is not constant with bias voltage, the differential conductance recorded with a spin-polarized tip contains spin information. In case of a constant spin polarization with bias voltage, the topographic tip stabilization levels out any variations of the tunneling current, and no contrast can be observed. As a spurious effect, the topographic images contain spin information similar to the constant current mode. Samples with strong variation of the density of states and spin polarization with bias are most suited for this technique. These are surfaces with surface states or thin films with quantized states. The contrast mode may be used with bulk and coated ferromagnetic or antiferromagnetic tips. This allows the influence of the magnetic stray field to be minimized and even allows operation in high magnetic fields. Its application to systems with a very inhomogeneous or unknown electronic structure is problematic. The technique offers high lateral resolution and has been used to image the magnetic structure of simple metallic ferromagnets and antiferromagnets.

The differential magnetic mode allows rigorous separation of topographic and spin information. The average tunneling current contains no spin information, and therefore constant current topographic images reflect the spin averaged density of states. Within the Jullière model, the differential magnetic signal, however, only contains spin information. It represents the local TMR between the tip and the sample surface, which is within the Julière model related to the integrated spin polarized density of states between the Fermi edge and the bias voltage. The technique can be applied to inhomogeneous samples. It has been used, however, only with bulk ferromagnetic tips for technical reasons. Further, tip preparation is more demanding, but the tip geometry fixes the direction of sensitivity. As the tip magnetization has to be switched periodically, thin film tips with high coercivities are not suited. A further limitation is that the application of a large magnetic filed affects the tip switching so that only studies in limited applied fields are possible. Using the above-mentioned simple Jullière model, the differential magnetic mode allows the measurement of the sample spin polarization independently of the existence of domains and is therefore well suited to study the TMR effect across vacuum barriers.

## 5 Beyond Magnetic Imaging

Spin-polarized STM has much more to offer than high-resolution imaging of the spin configuration. Like STM, it can be used to gain information of the density of states and fundamental mechanisms of tunneling. In contrast to STM, Sp-STM may give spin-resolved information. Two examples of such studies are discussed in the below.

### *5.1 Vacuum Tunneling Versus Tunneling Across an Insulator*

Spin-polarized tunneling has been of particular interest in the last years due to its application to magnetic tunnel devices. In the pioneering work of Jullière on

planar junctions, the dependence of the tunneling resistance on the relative orientation of the electrode magnetization was related to the spin polarization of the density of states at the Fermi energy [7]. The TMR effect, however, is still far from being completely understood. A particular aspect, namely, that the TMR in planar junctions with oxide barriers decreases with increasing bias voltage, is still puzzling. Due to its technological importance, many studies have been devoted to this. In the early work of Jullière, a bias as small as 3 mV was needed to halve the value of the TMR. With increased control of the preparation, this value increased up to 700 mV over the years [46]. Many models have been proposed to explain this behavior. First, biasing of the junctions leads to elastic tunneling of electrons mostly from the Fermi energy of the negative electrode into empty states of the positive electrode. Since the spin polarization of the empty states depends in general on the energy, it should cause variations of the TMR due to density-of-states effects. Via this mechanism, information on the spin-dependent density of states can be obtained. Second, hot electrons from the positive electrode might be scattered in a spin-dependent way at defects in the amorphous barriers [47] or might create magnons [48]. The latter mechanisms reduce the spin polarization and, consequently, the TMR.

To elucidate the mechanism, difficulties related to the complex structure of the tunnel junctions (polycrystalline electrodes, poorly characterized amorphous barriers) have to be overcome to perform well-defined experiments and to allow comparison with theoretical results. Here, Sp-STM measurements of the voltage dependence of the TMR across the vacuum barrier, where effects due to impurities in the spacer are obviously not present, are helpful. Magnon creation and the density-of-states effect are in principle still present. Further, theoretical modeling of spin-polarized tunneling across a well-defined vacuum barrier is feasible. Measurements of the TMR were carried out in ultrahigh vacuum with a Sp-STM between an amorphous tip and a Co(0001) sample. During the measurement, the bias voltage was varied while keeping the tip at a fixed position and measuring the averaged tunneling current $I_t$ and the modulated current $\Delta I$. The TMR, defined as the asymmetry $\delta$ of the tunneling currents observed for parallel and antiparallel magnetization alignment ($P$ and $AP$), was obtained from the ratio of these two currents. The measured TMR (Figure 10(a)) obtained with the tip stabilized at 1 V, 1 nA, is almost constant with bias voltage. This is in contrast to the case of planar tunnel junctions with amorphous spacers. If spin-dependent scattering at magnons was the dominant mechanism for the drop of the TMR, a similar decrease of the TMR with bias voltage should also be present in our case. Its absence, however, indicates that this mechanism is not dominant.

Additional insight into the mechanisms of spin-polarized tunneling can be gained by first-principle calculations of the TMR. Several modern approaches beyond the simple Jullière model exist. Especially successful is the scheme proposed by MacLaren and coworkers [49] for planar tunnel junctions. In this model, the electronic structures of the electrode and the barrier are treated by first principle calculations and the current is modelled as a coherent scattering process of electrons from one electrode into the other. These calculations for Co(0001)

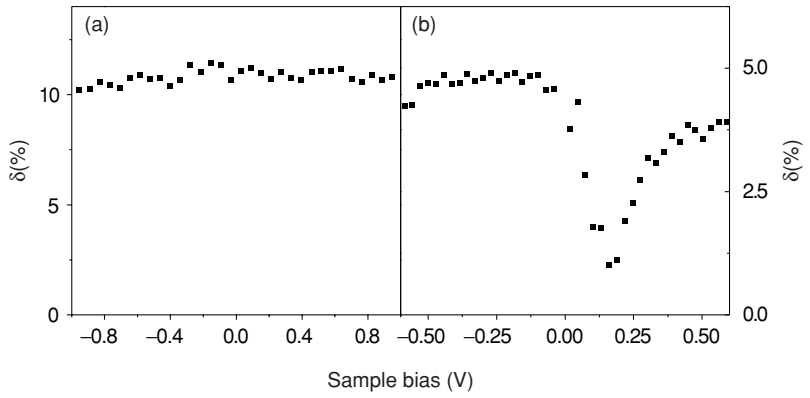


FIGURE 10. Tunnel magnetoresistance $\delta$ of a clean Co(0001) surface versus bias voltage, obtained with a magnetic tip stabilized at **(a)** 1 V, 1 nA, and **(b)** 100 mV, 1 nA.

junctions reveal a similar behavior as the Sp-STM experiments. Using semi-infinite Co(0001) electrodes, conductances $G$ for parallel and antiparallel alignment were computed [50]. As usual, the calculated conductances (Figure 11(a)) for parallel alignment are larger than those for antiparallel alignment of the electrode magnetizations. Further, the tunneling conductances at $d = 2d_0$ separation is almost two orders of magnitude larger than those for $3d_0$ ($d_0 = 2.035$ Å, the Co interlayer distance), as expected for vacuum tunneling. In agreement with the experimental results for large separations, the TMR is almost constant [50].

For small barrier widths, tunneling via surface states could become important in STM experiments [19]. This might lead to pronounced changes in the TMR. Figure 10(b) presents the experimental TMR versus bias voltage obtained at a smaller

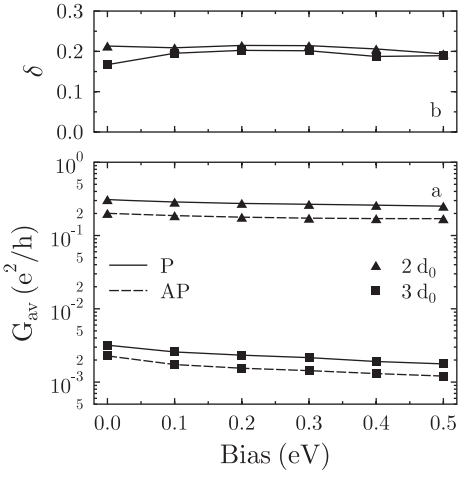


FIGURE 11. Theoretical spin-dependent tunneling through Co(0001) planar junctions. **(a)** Conductances $G$ for parallel (P) and antiparallel (AP) magnetization alignment at various barrier widths $d$ *vs* bias voltage. **(b)** Tunnel magneto-resistance $\delta$ obtained from the data shown in (a).

tip-sample separation (feedback conditions: 100 mV, 1 nA). For negative bias, a constant TMR is still observed. For positive bias, however, a strong dip at 200 mV is present. According to Jullière's model, one can speculate that the dip is related to majority states which reduce the minority-dominated spin polarization at this energy. Indeed, inverse photoemission measurements revealed a majority surface state of Co(0001) at $\approx 0.2$ eV [51] which is also found in the calculations. At small tip-sample separations, the tunneling probability through this surface state can be enhanced and thus would decrease significantly the TMR. The density-of-states mechanism qualitatively explains the constant TMR for large tip-sample separations and the minimum at small tip-sample separations. The dip at 200 mV does not show up in our transport calculations because surface states do not contribute to the conductance in that model. It is, however, conceivable that the surface state contributes to the tunneling current through scattering at steps or defects [50].

### *5.2 Spin-Orbit Mixing as a Function of Magnetization Direction*

Sp-STM in the spectroscopic mode may also be used to study the electronic structure of ferromagnets as a function of the magnetic configuration. Due to the spin-orbit interaction, the band structure of a ferromagnet depends on the direction of magnetization [52] and the degeneracies of the 3d-bands can be lifted [53]. Sp-STM in the spectroscopic mode allows the local density of states in areas of different sample magnetization to be compared. By this the minute changes in the density of states induced by the spin-orbit interaction may be resolved. Figure 12a shows the topographic image of $\approx$1.75 ML of Fe on W(110). The DL stripes show a stripe domain pattern of domains magnetized up and down out of the stripe plane, as Figure 12(b) reveals [54]. Fe coated tips image the in-plane magnetized domain walls between the stripe domains as alternating bright and dark lines (see Figure 12(c)). Maps of the differential conductance taken at certain bias voltages with bare W tips, however, also show these in-plane domain walls (see Figure 12(d)). They appear as dark lines, i.e. do not contain information on the in-plane direction of the magnetization in the walls, but indicate whether the magnetization is locally out-of-plane (gray) or in-plane (black). Figure 12(e) shows in all detail the minute changes of the differential conductivity upon reorientation of the magnetization from in-to out-of plane. Ab initio calculations revealed that the differences are due to changes of the mixing of the $d_{xy}$ and the $d_{z^2}$ states depending on the magnetization direction [54]. This example shows the high potential of Sp-STM to study the density of states in ferromagnets. The accuracy is high enough to resolve the weak impact of the spin-orbit interaction on the density of states.

## 6 Outlook

With the successful operation of Sp-STM in all three modes proposed by Pierce, Sp-STM has become an established technique. It is now widely used by several

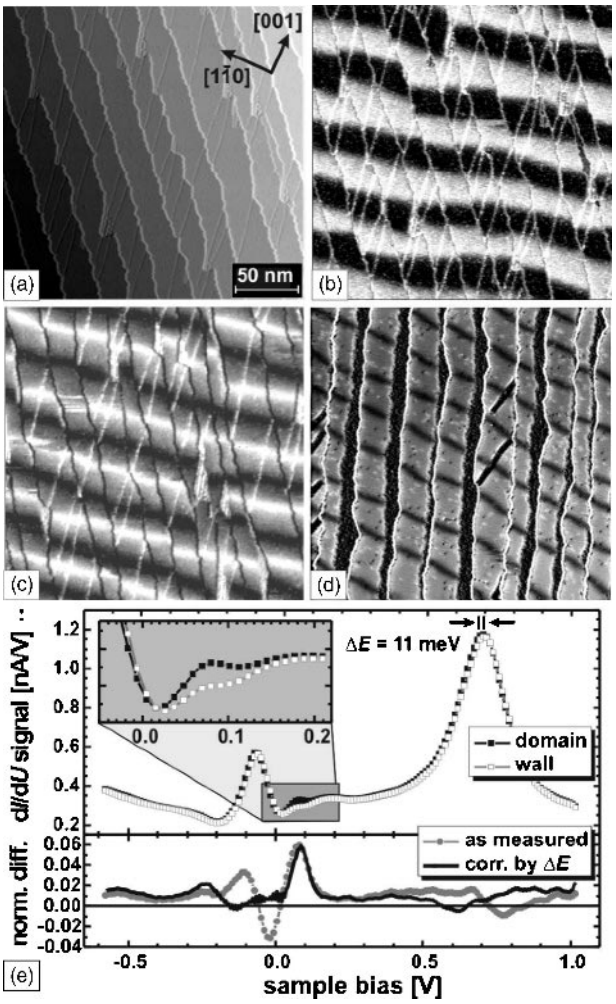


FIGURE 12. **(a)** Topographic image of $\approx 1.75$ mL Fe on W(110). Sp-STM maps of the local differential conductivity using **(b)** a Gd-coated tip ($U = 0.7$ V) and **(c)** a Fe tip ($U = 0.05$ V) show a stripe domain pattern in the perpendicularly magnetized DL stripes. They appear as alternating bright and grey areas in (b). The domain walls between the stripe domains are resolved as alternating black and white lines in (c). **(d)** Map of the differential conductance recorded with uncoated W tips ($U = 0.05$ V) where the domain walls appear darker. **(e)** Comparison of the differential conductance recorded on domains and domain walls as a function of sample bias. Figure kindly provided by M. Bode.

groups in Europe, Asia, and America. Its potential for high-resolution magnetic imaging has only been exploited with a small number of systems. More studies on all kinds of systems will give a deeper understanding of magnetism on the nanometer scale. Sp-STM is also the method of choice to investigate the spin structure

of antiferromagnetic surfaces. The real-space information gained is complementary to the information already available from magnetic scattering techniques like neutron scattering. Sp-STM allows us to tackle new classes of problems in antiferromagnets: frustrations and aperiodic structures. Finally, Sp-STM may be used to investigate the density of states and their spin polarization at the same time. Because of this, it has the potential to become a valuable tool for electron spectroscopy—beyond high-resolution magnetic imaging.

## *References*

1. J. Tersoff and D. R. Hamann, Phys. Rev. Lett. **50**, 1998 (1983).
2. J. Tersoff and D. R. Hamann, Phys. Rev. B **31**, 805 (1985).
3. G. Binning, H. Rohrer, Ch. Gerber, and E. Weibel, Appl. Phys. Lett. **40**, 178 (1982).
4. G. Binning, H. Rohrer, Ch. Gerber, and E. Weibel, Phys. Rev. Lett. **49**, 57 (1982).
5. N. Müller, W. Eckstein, W. Heiland, and W. Zinn, Phys. Rev. Lett. **29**, 1651 (1972).
6. M. Landolt and Y. Yafet, Phys. Rev. Lett. **40**, 1401 (1978).
7. M. Jullière, Phys. Lett. **54A**, 225 (1975).
8. J. C. Slonczewski, Phys. Rev. B **39**, 6995 (1989).
9. T. Miyazaki and N. Tezuka, J. Magn. Magn. Mater. **139**, L231 (1995).
10. D. T. Pierce, Physica Scripta **38**, 291 (1988).
11. Y. Suzuki, W. Nabhan, and K. Tanaka, Appl. Phys. Lett. **71**, 3153 (1997).
12. S. F. Alvarado and P. Renaud, Phys. Rev. Lett. **68**, 1387 (1992).
13. S. Heinze, P. Kurz, D. Wortmann, G. Bihlmayer, and S. Blügel, Appl. Phys. A **75**, 25 (2002).
14. R. Wiesendanger, H. J. Güntherodt, G. Güntherodt, R.J. Gambino, and R. Ruf, Phys. Rev. Lett. **65**, 247 (1990).
15. S. Blügel, D. Pescia, and P.H. Dederichs, Phys. Rev. B **39**, 1392 (1989).
16. M. Kleiber, M. Bode, R. Ravlic, and R. Wiesendanger, Phys. Rev. Lett. **85**, 4606 (2000).
17. S. Heinze, M. Bode, A. Kubetzka, O. Pietzsch, X. Nie, S. Blügel, and R. Wiesendanger, Science **288**, 1805 (2000).
18. H. Yang, A. R. Smith, M. Prikhodko, and W.R.L. Lambrecht, Phys. Rev. Lett. **89**, 226101 (2002).
19. J. A. Stroscio, D. T. Pierce, A. Davies, R. J. Celotta, and M. Weinert, Phys. Rev. Lett. **75**, 2960 (1995).
20. M. Bode, M. Getzlaff, and R. Wiesendanger, Phys. Rev. Lett. **81**, 4256 (1998).
21. H. J. Elmers, J. Hauschild, and U. Gradmann, Phys. Rev. B **59** 3688 (1998).
22. O. Pietzsch, A. Kubetzka, M. Bode, and R. Wiesendanger, Phys. Rev. Lett. **84**, 5212 (2000).
23. B. Heinrich, A. S. Arrott, C. Liu, and S. T. Purcell, J. Vac. Sci. Technol. A **5**, 1935 (1987).
24. T.G. Walker and H. Hopster, Phys. Rev. B **48**, 3563 (1993).
25. T.K. Yamada, M.M.J. Bischoff, G. M. M. Heijnen, T.Mizoguchi, and H. van Kempen, Phys. Rev. Lett. **90**, 056803 (2003).
26. A. Kubetzka, M. Bode, O. Pietzsch, and R. Wiesendanger, Phys. Rev. Lett. **88**, 057201 (2002).
27. R. Ravlic, M. Bode, and R. Wiesendanger, Journ. Phys., Cond. Matter **15**, 2513 (2003).
28. A. Yamasaki, W. Wulfhekel, R. Hertel, S. Suga, and J. Kirschner, Phys. Rev. Lett. **91**, 127201 (2003).

29. M. Bode, O. Pietzsch, A. Kubetzka, and R. Wiesendanger, Phys. Rev. Lett. **92**, 067201 (2004).
30. O. Pietzsch, A. Kubetzka, M. Bode, and R. Wiesendanger, Phys. Rev. Lett. **92**, 057202 (2004).
31. M. Johnson and J. Clarke, J. Appl. Phys. **67**, 6141 (1990).
32. W. Wulfhekel and J. Kirschner, Appl. Phys. Lett. **75**, 1944 (1999).
33. J. Unguris, M. R. Scheinfein, R. C. Celotta, and D.T. Pierce, Appl. Phys. Lett. **55**, 2553 (1989).
34. H. F. Ding, W. Wulfhekel, C. Chen, J. Barthel, and J. Kirschner, Mater. Sci. and Engineering B **84**, 96 (2001).
35. H. F. Ding, W. Wulfhekel, and J. Kirschner, Europhys. Lett. **57**, 100 (2002).
36. U. Schlickum, W. Wulfhekel, and J. Kirschner, Appl. Phys. Lett. **83**, 2016 (2003).
37. S. Andrieu, E. Foy, H. Fischer, M. Alnot, F. Chevrier, G. Krill, and M. Piecuch, Phys. Rev. B **58** 8210 (1998).
38. A. Berger and H. Hopster, Phys. Rev. Lett. **73**, 193 (1994).
39. A. Berger A and E. E. Fullerton, J. Magn. Magn. Mater **165**, 471 (1997).
40. U. Schlickum, N. Janke-Gilman, W. Wulfhekel, and J. Kirschner, Phys. Rev. Lett. **92**, 107203 (2004).
41. M. Pajda, J. Kudrnovský, I. Turek, V. Drchal, and P. Bruno, Phys. Rev. B **64**, 174402 (2001).
42. W. Wulfhekel, H. F. Ding, G. Steierl, M. Vazquez, P. Marin, A. Hernando, and J. Kirschner, Appl. Phys. A **72**, 463 (2001).
43. M. Bode and R. Wiesendanger, In: *Magnetic Microscopy of Nanostructures*, ed. by H. Hopster, H.P. Oepen (Springer, Berlin Heidelberg New York, 2004), p. 205.
44. T.K. Yamada, M.M.J. Bischoff, T. Mizoguchi, and H. van Kempen, Appl. Phys. Lett. **82**, 1437 (2003).
45. W. Wulfhekel, R. Hertel, H. F. Ding, G. Steierl, and J. Kirschner, J. Magn. Magn. Mater. **249**, 368 (2002).
46. H. Boeve, E. Girgis, J. Schelten, J. De Boeck, and G. Borghs, Appl. Phys. Lett. **76**, 1048 (2000).
47. J. Zhang and R. White, J. Appl. Phys. **83**, 6512 (1998).
48. J. S. Moodera, J. Nowak, and R. J. M. van de Veerdonk, Phys. Rev. Lett. **80**, 2941 (1998).
49. J. M. MacLaren, X.- G. Zhang, W. H. Butler, and X. Wang, Phys. Rev. B **59**, 5470 (1999).
50. H. F. Ding, W. Wulfhekel, J. Henk, P. Bruno, and J. Kirschner, Phys. Rev. Lett. **90**, 116603 (2003).
51. C. Math, J. Braun, and M. Donath, Surf. Sci. 482–485, 556 (2001).
52. R. Wu, and A. J. Freeman, J. Magn. Magn. Mater. **200**, 498 (1999).
53. A. Lessard, T. H. Moos, and W. Hübner, Phys. Rev. B **56**, 2594 (1997).
54. M. Bode, S. Heinze, A. Kubetzka, O. Pietsch, X. Nie, G. Bihlmayer, S. Blügel, and R. Wiesendanger, Phys. Rev. Lett. **89**, 237205 (2002).